Journal of Catalysis 352 (2017) 142–154

Contents lists available at ScienceDirect

Journal of Catalysis

journal homepage: www.elsevier.com/locate/jcat

Photophysical, transport and structure properties of $Tl_{10}Hg_3Cl_{16}$ single crystals: Novel photocatalytic water-splitting solar-to-hydrogen energy conversion

A.H. Reshak *

New Technologies—Research Centre, University of West Bohemia, Univerzitni 8, 306 14 Pilsen, Czech Republic
School of Material Engineering, University Malaysia Perlis, 01007 Kangar, Perlis, Malaysia

ARTICLE INFO

Article history:
Received 10 April 2017
Revised 23 April 2017
Accepted 24 April 2017

Keywords:
Photocatalysts
Transport properties
Ultrafast scintillator materials
mBJ

ABSTRACT

The photocatalytic, transport, photophysical, and structural properties of $Tl_{10}Hg_3Cl_{16}$ single crystals are investigated by means of density functional theory in order to investigate its suitability to be used as an active photocatalyst. The calculation show that this compound possesses a narrow direct band gap. The obtained values of the fundamental energy band gap are about 0.82 eV (LDA), 0.88 eV (PBE-GGA), and 0.97 eV (mBJ). The absorption edge of $Tl_{10}Hg_3Cl_{16}$ occurs at $\lambda = 742.3$ nm, and the optical band gap is estimated to be 1.67 eV. For use in photocatalytic water splitting, the optical band gap of the photocatalyst material must be sufficiently large to overcome the endothermic character of the water-splitting reaction, i.e., higher than 1.23 eV therefore, $Tl_{10}Hg_3Cl_{16}$ (Eg = 1.67 eV) is expected to be an active photocatalyst. The calculated density of states reveals the orbitals that form the conduction band minimum and the valence band maximum, and the existence of hybridization. The transport properties are calculated to investigate the suitability of $Tl_{10}Hg_3Cl_{16}$ as a thermoelectric power generator, as an active photocatalyst for clean energy resources, and as an ultrafast scintillator for medical imaging.

1. Introduction

Ultrafast scintillators are needed for medical imaging, nuclear physics, and high-energy physics [1]. The use of near-edge emission from a material with fast electron–hole recombination is possible. It has been reported that by n-doping ZnO and CdS with Ga and In under reducing conditions, quenching could be reduced and edge emission with high luminosity could be realized [1]. Among such materials, $Tl_{10}Hg_3Cl_{16}$ is a potential candidate for novel scintillators [2], ionizing radiation detectors [3], ion-selective electrodes [4–6], and temperature sensors [7]. $Tl_{10}Hg_3Cl_{16}$ contains two heavy elements (Hg and Tl) [8,9]. Therefore, a careful analysis of their crystal structure is essential to understand the structure-to-property relationship of the compound. The structure of $Tl_{10}Hg_3Cl_{16}$ (tetragonal; space group $I4/m$; $a = 849{,}0(2)$ pm, $c = 2372{,}9(6)$ pm) was determined by X-ray structure analysis [2]. This compound consists of $HgCl_4$ tetrahedra and linear Cl—Hg—Cl units, which are completed by four additional chlorides as distorted (2 + 4) $HgCl_6$ octahedra [2]. Recently, Khyzhun et al. have grown a single crystal of the ternary halide $Tl_{10}Hg_3Cl_{16}$ using the Bridgman–Stockbarger method [10]. They have reported that the surface of $Tl_{10}Hg_3Cl_{16}$ is very sensitive to Ar^+ ion bombardment, which causes significant changes of the element stoichiometry, resulting in an abrupt decrease of Hg content in the top surface layers [10]. This treatment makes the top surface of $Tl_{10}Hg_3Cl_{16}$ free of Hg and hence free of risk, which makes it possible to use in advanced technological applications [11–13].

Photocatalytic water splitting is one of the most promising strategies for clean and renewable solar-to-hydrogen energy conversion [14–20]. The development of visible-light-responsive photocatalysts has attracted several workers in recent years [21]. Among the various types of visible-light-responsive photocatalysts, $Tl_{10}Hg_3Cl_{16}$ could be considered because of its optical gap (1.67 eV, $\lambda = 742.3$ nm), well matched with the solar spectrum, and its sufficiently negative conduction band potential for reduction of H^+/H_2 [22–24].

Thermoelectric power generators are a good alternative solution for energy and environment problems, which can directly convert heat into electricity [25]. Tremendous research work has been done on thermoelectric materials to enhance their thermoelectric properties for technological applications [26–35]. The development of thermoelectric materials has attracted a great deal of

* Address: New Technologies—Research Centre, University of West Bohemia, Univerzitni 8, 306 14 Pilsen, Czech Republic. Fax: +420 386 361255.
E-mail address: maalidph@yahoo.co.uk

http://dx.doi.org/10.1016/j.jcat.2017.04.028
0021-9517/

interest due to their significant potential applications, ranging from clean energy to photon-sensing devices. Thermoelectric materials can make a significant contribution to solving global sustainable energy problems. These materials are used not only in generating electricity from waste heat but also as solid-state Peltier coolers [36].

To the best of our knowledge, no comprehensive work either on experimental data on transport and optical properties or on first principles calculations of the structural, electronic, transport, photocatalytic, and optical properties of $Tl_{10}Hg_3Cl_{16}$ have appeared in the literature. Therefore, as a natural extension to previous experimental work of Brodersen et al. [2], a detailed depiction of the electronic structure, transport, photocatalytic, and optical properties of $Tl_{10}Hg_3Cl_{16}$ using a full potential method is timely and would bring us important insight into the origin of the band structure, density of states, and photocatalytic and photophysical properties. Hence, it is very important to use a full potential method based on density functional theory (DFT). The full-potential method [37], with different types of exchange correlation (XC) potentials, namely the local density approximation (LDA) [38], general gradient approximation (PBE-GGA) [39], and modified Becke–Johnson potential (mBJ) [40], is used to ascertain the influence of the XC on the resulting band gap and hence on the ground state properties of $Tl_{10}Hg_3Cl_{16}$.

In this work, ab inito calculations from first- to second-principles methods are performed to investigate the suitability of $Tl_{10}Hg_3Cl_{16}$ as an active photocatalyst in the visible light region.

2. Details of calculations

The full-potential linear augmented plane wave plus local orbitals (FPLAPW + lo) method as implemented in WIEN2k code [37] within the generalized gradient approximation (PBE-GGA) [39] are used to optimize the experimental structural geometry of $Tl_{10}Hg_3Cl_{16}$ [2]. The criterion for convergence of maximum force among atoms is 1 mRy/a.u., at which the structural geometry is relaxed. The resulting structural geometry of $Tl_{10}Hg_3Cl_{16}$ in comparison with the experimental data [2] is given in Table 1. The optimized crystal structure of $Tl_{10}Hg_3Cl_{16}$ is depicted in Fig. 1. The structure consists of $HgCl_4$ tetrahedra and linear Cl—Hg—Cl units, which are completed by four additional chlorides to form distorted (2 + 4) $HgCl_6$ octahedra [2]. We have used the optimized crystal structure as input data to calculate the electronic band structure, density of states, electronic charge density distribution, and photocatalytic and optical properties using different types of exchange correlation (XC) potentials to ascertain the influence of the XC on the resulting properties. Furthermore, we have calculated the transport properties based on the semiclassical Boltzmann theory, as incorporated into the BoltzTraP code [41] within the limits of Boltzmann theory [42–44] and the constant relaxation time approximation [41]. We have used a mesh of 800 $\vec{k}$ points in the irreducible Brillouin zone (IBZ) to achieve self-consistency. The self-consistent calculations are converged, since the total energy of the system is stable within 0.00001 Ry. The photophysical, transport, photocatalytic, and structure properties are determined within 20,000 $\vec{k}$ points in the IBZ. In the recent years, due to the improvement of computational technologies, it has been proven that first-principles calculation is a strong and useful tool for predicting the crystal structure and properties related to the electron configuration of a material before its synthesis [45–55]. We should emphasize that several researchers have used first-principles calculation to explore new photocatalysts and found good agreement with experimental results [56–62].

3. Results and discussion

3.1. Electronic band structure and density of states

Schematic diagrams of charge transfer and photocatalytic mechanism of $Tl_{10}Hg_3Cl_{16}$ are shown in Fig. 2a. When the photocatalyst absorbs radiation from sunlight, it produces electron and hole pairs. The electron of the valence band becomes excited when illuminated by light. The excess energy of this excited electron promotes the electron to the conduction band, creating a negative electron (e^-) and positive hole (h^+) pair. This stage is referred as the semiconductor's photoexcitation state. Since the photocatalytic activities are directly related to the material's electronic structure [63], the electronic band structure along the high-symmetry directions of the first BZ and the total density of states of the tetragonal $Tl_{10}Hg_3Cl_{16}$ are calculated to explore the bands' dispersion and the nature of the fundamental energy band gap, as shown in Fig. 2b. We set the zero point of energy (Fermi level, E_F) at the valence band maximum (VBM). It has been found that the conduction band minimum (CBM) and VBM are located along the Z and Γ directions, resulting in a direct band gap. The calculated value of the fundamental energy band gap is about 0.82 eV (LDA), 0.88 eV (PBE-GGA), or 0.97 eV (mBJ). These values are much higher than 0.22 eV, which was obtained from previous calculations using the full-potential linear muffin-tin orbital (FP-LMTO) method within LDA. It is well known that both LDA and GGA underestimate the energy band gap [64], and since the experimental value has not yet been reported, we performed the calculation within the mBJ. The mBJ, a modified Becke–Johnson potential, allows the calculation of band gaps with accuracy similar to that of the very expensive GW calculations [40]. It is a local approximation to an atomic "exact-exchange" potential and a screening term. In Fig. 2c, we enlarge the electronic band structure to visualize the bands around the Fermi level that govern the energy band gap. Since mBJ succeeds by a large amount in correcting the calculated energy gap to be closer to the expected experimental one, we select to show

Table 1
Crystallographic data for $Tl_{10}Hg_3Cl_{16}$ (tetragonal; space group *I*4/*m*).

Element	Wyckoff	*x* exp.	*x* opt.	*y* exp.	*y* opt.	*z* exp.	*z* opt.
Hg(1)	2a	0.0	0.0	0.0	0.0	0.0	0.0
Hg(2)	4d	0.0	0.0	0.5	0.5	0.25	0.25
Tl(1)	16i	0.1689(3)	0.1677	0.3641(3)	0.3637	0.0896(1)	0.0889
Tl(2)	4e	0.0		0.0		0.2581(3)	0.2578
Cl(1)	4e	0.0		0.0		0.0995(12)	0.0991
Cl(2)	8 h	0.3315(22)	0.3311	0.1526(19)	0.1521	0.0	0.0
Cl(3)	4e	0.0		0.0		0.3971(17)	0.3968
Cl(4)	16i	0.2404(16)	0.2400	0.1624(13)	0.1617	0.1865(7)	0.1860

Notes: The experimental lattice constants are $a = b = 8.490(2)$ Å and $c = 23.729(6)$ Å [2].
the optimized lattice constants are $a = b = 8.411$ Å and $c = 23.688$ Å. The experimental atomic positions, in comparison with the optimized atomic position after we minimized the forces acting on the atoms, are less than 1 mRy/a.u.

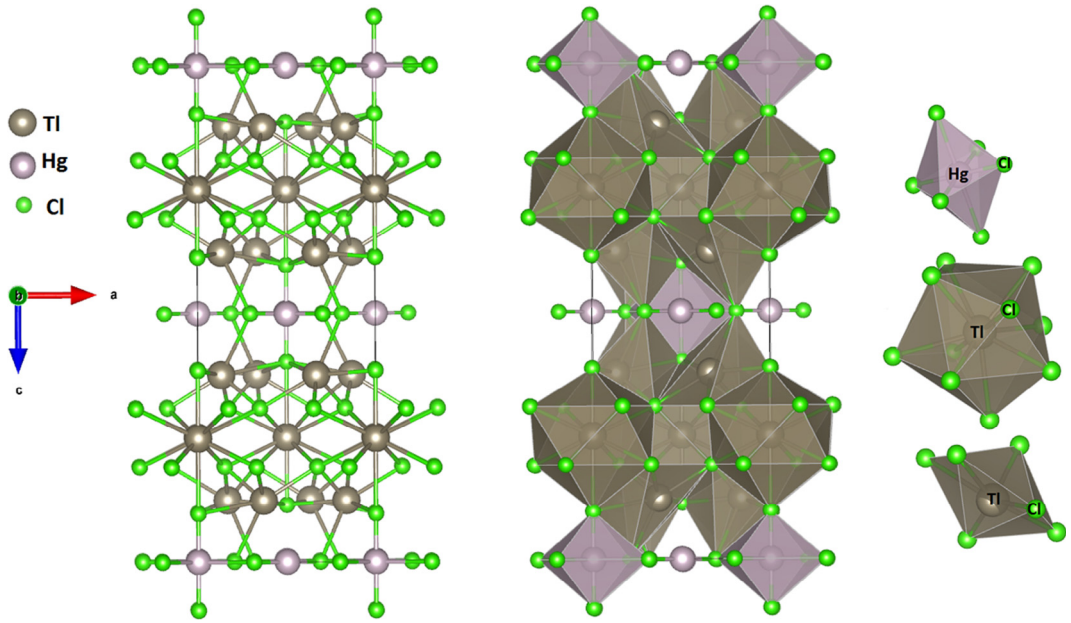

Fig. 1. Crystal structure of a $Tl_{10}Hg_3Cl_{16}$ single crystal, which show that the Tl atoms have octahedral and tetrahedral surroundings and the Hg atoms have only tetrahedral surroundings. The structure consists of $HgCl_4$ tetrahedra and linear Cl—Hg—Cl units, which are completed by four additional chlorides to distorted (2 + 4) $HgCl_6$ octahedra. Also, it shows the $TlCl_{10}$ decahedra, $TlCl_6$ hexagons, and $HgCl_6$ octahedra.

the results obtained by mBJ, as illustrated in Fig. 2b and c, which confirm the fundamental energy band gap value of about 0.97 eV.

Further, the angular-momentum-resolved projected density of states (PDOS) using LDA, PBE-GGA, and mBJ is obtained from the calculated band structure by means of the modified tetrahedron method. The calculated PDOS using mBJ is shown in Fig. 3a–i. The PDOS enables us to identify the angular momentum characters of the various structures the VBM is formed from Cl3-*p*, Cl4-*p*, Tl1-*s*, Tl2-*p*, and Hg2-*d* states, whereas the CBM is originated from Hg2-*s*/*d* and Cl2-*p* states. The energy region extending from −10.0 eV up to E_F is originated from Hg1-*s*/*p*/*d*/*f*, Hg2-*s*/p/*d*/*f*, Tl1-*s*/*d*/*f*, Tl2-*s*/*d*/*f*, Cl1-*s*/*p*, Cl2-*s*/*p*, Cl3-*s*/*p*, and Cl4-*s*/*p* states, while the energy region from the CBM and above is mainly originated from Hg1-*s*/*p*/*f*, Hg2-*s*/*p*/*f*, and Tl1-*p*/*d*/*f* with small contribution from Cl1,2,3,4-*s*/*p* states. It has been noticed that there exist some weak/strong hybridizations between the states, which may lead to partly covalent bonding. The covalence degree depends on the strength/weakness of the hybridization. We should emphasize that our calculated partial density of states for $Tl_{10}Hg_3Cl_{16}$ is in concordance with those in other compounds containing Tl, Hg, and Cl ions [65–67].

With the aid of the calculated angular momentum decomposition of the atoms' projected electronic density of states (Fig. 3a–c) we can elucidate the chemical bonding characters. In the valence bands between −8.0 eV and E_F, we have obtained a total number of electrons/eV (e/eV) for the orbitals in each atom of $Tl_{10}Hg_3Cl_{16}$ as follows: Hg2 atom 14 e/eV, Hg1 atom 100 e/eV, Tl2 atom 3.0 e/eV, Cl1 atom 25 e/eV, Cl2 atom 9 e/eV, Cl3 atom 5 e/eV, and Cl4 atom 20 e/eV. It is clear that some electrons from Hg, Cl, and Tl atoms are transferred into valence bands and contribute to covalence interactions between the atoms, according to the contribution of each atom to the valence bands. The strength/weakness of the covalence interactions arises from the degree of hybridization and the electronegativity differences between the atoms. Thus, the angular momentum decomposition of the atoms' projected electronic density of states helps us to analyze the nature of the bonds, following the classical chemical concept. This concept is very useful in classifying compounds into different categories with respect to different chemical and physical properties.

3.2. Valence electronic charge density

To support the above statement and to gain further understanding of the bonding features, we have calculated the valence charge density distributions. To investigate the anisotropic nature of chemical bonding in $Tl_{10}Hg_3Cl_{16}$, we have calculated and presented the electronic charge density distribution in two crystallographic planes, namely (1 0 0) and (1 0 1), as shown in Fig. 4a–c. The crystallographic planes show clear maps for the electronic charge surrounding the atoms. The crystallographic plane (1 0 0) shows only Hg and Cl atoms, and the Hg atoms have only tetrahedral surroundings. The crystallographic plane (1 0 1) shows Tl, Hg, and Cl atoms. The Hg atoms have only tetrahedral surroundings and the Tl atoms have octahedral and tetrahedral surroundings.

The nature of bonding among the atoms of $Tl_{10}Hg_3Cl_{16}$ can be explained using the map of the electronic charge density distribution. The transfer of charge between the anion and cation can be utilized to explain the ionic character, whereas sharing the charge between anion and cation is related to the covalent character. It has been found that Hg and Cl atoms form partial ionic/covalent bonding in the linear Cl—Hg—Cl units. The unconnected Tl atoms form an ionic bond, while the Cl atom that is far from the Tl atom also forms an ionic bond. According to the Pauling scale, the electronegativities of Cl, Hg, and Tl are 3.16 > 2.00 > 1.62, which shows that the Cl atom possesses the highest electronegativity in $Tl_{10}Hg_3Cl_{16}$. For the description of the bonding character, the difference of the electronegativity (X_A-X_B) is crucial [68], where X_A and X_B denote the electronegativity of the A and B atoms in general. With increasing difference, the ionic character of the bonding increases. The percentage of ionic character (P) of bonding can be obtained following the relation [68]

$$P(\%) = 16(X_A\text{-}X_B) + 3.5(X_A\text{-}X_B)^2. \quad (1)$$

The calculated values of the ionic character are given in Table 2. It is clear that the Tl in the $TlCl_{10}$ decahedra and $TlCl_6$ hexagons forms mostly covalent and partially ionic bonds with the surrounding Cl atoms also, the Hg atom in the $HgCl_6$ octahedron forms mostly covalent and partially ionic bonds with the surrounding Cl atoms, whereas Hg atoms form very strong covalent bonds with

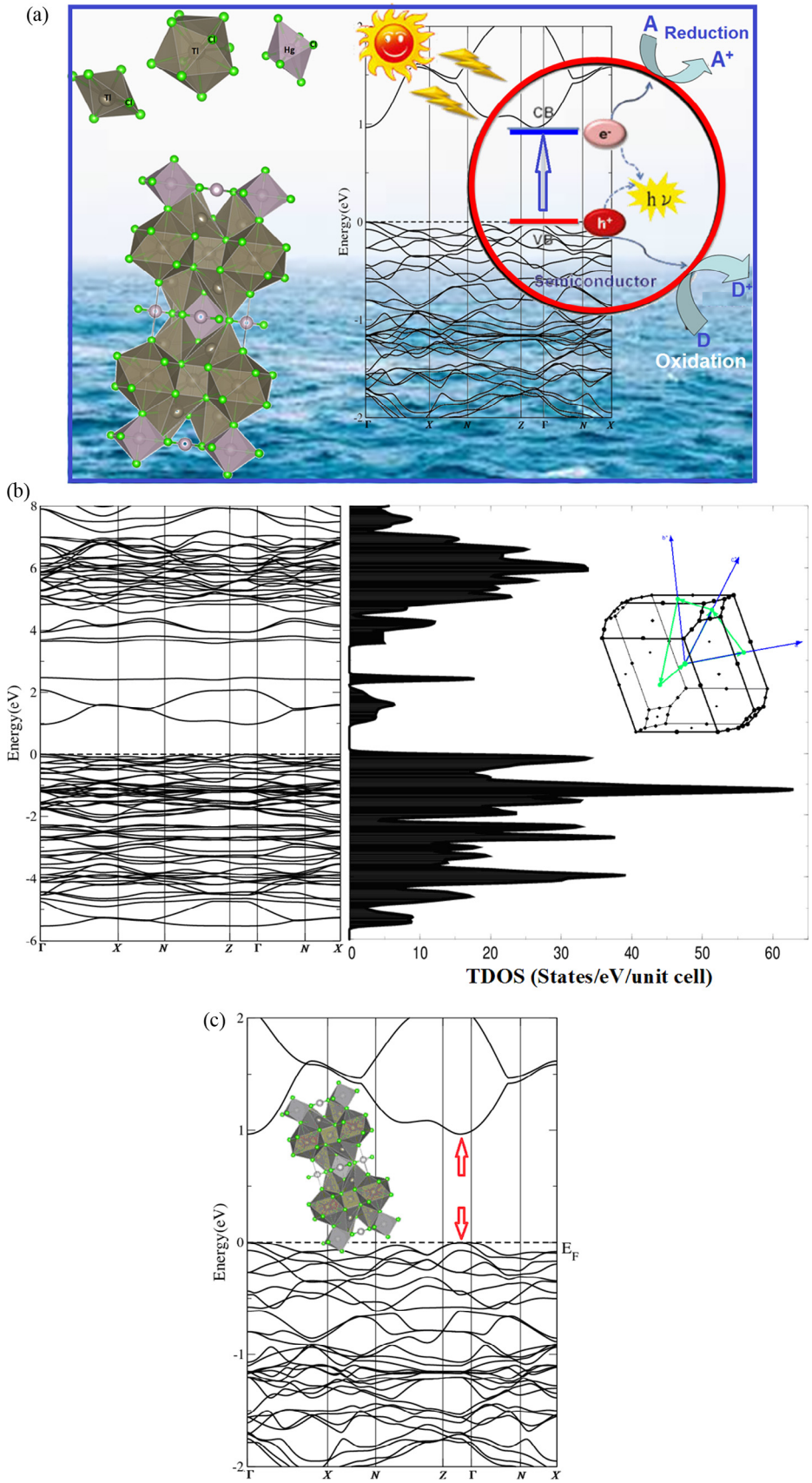

Fig. 2. (a) Schematic diagrams of charge transfer and photocatalytic mechanism of $Tl_{10}Hg_3Cl_{16}$. When the photocatalyst absorbs radiation from sunlight, it produces electron and hole pairs. The electron of the valence band becomes excited when illuminated by light. The excess energy of this excited electron promotes it to the conduction band, creating a negative electron (e^-) and positive hole (h^+) pair. This stage is referred as the semiconductor's photoexcitation state. (b) The calculated electronic band structure along with the calculated total density of states and the first Brillouin zone. (c) The enlarged electronic band structure, which clearly show the conduction band minimum, the valence band maximum, and the energy band gap.

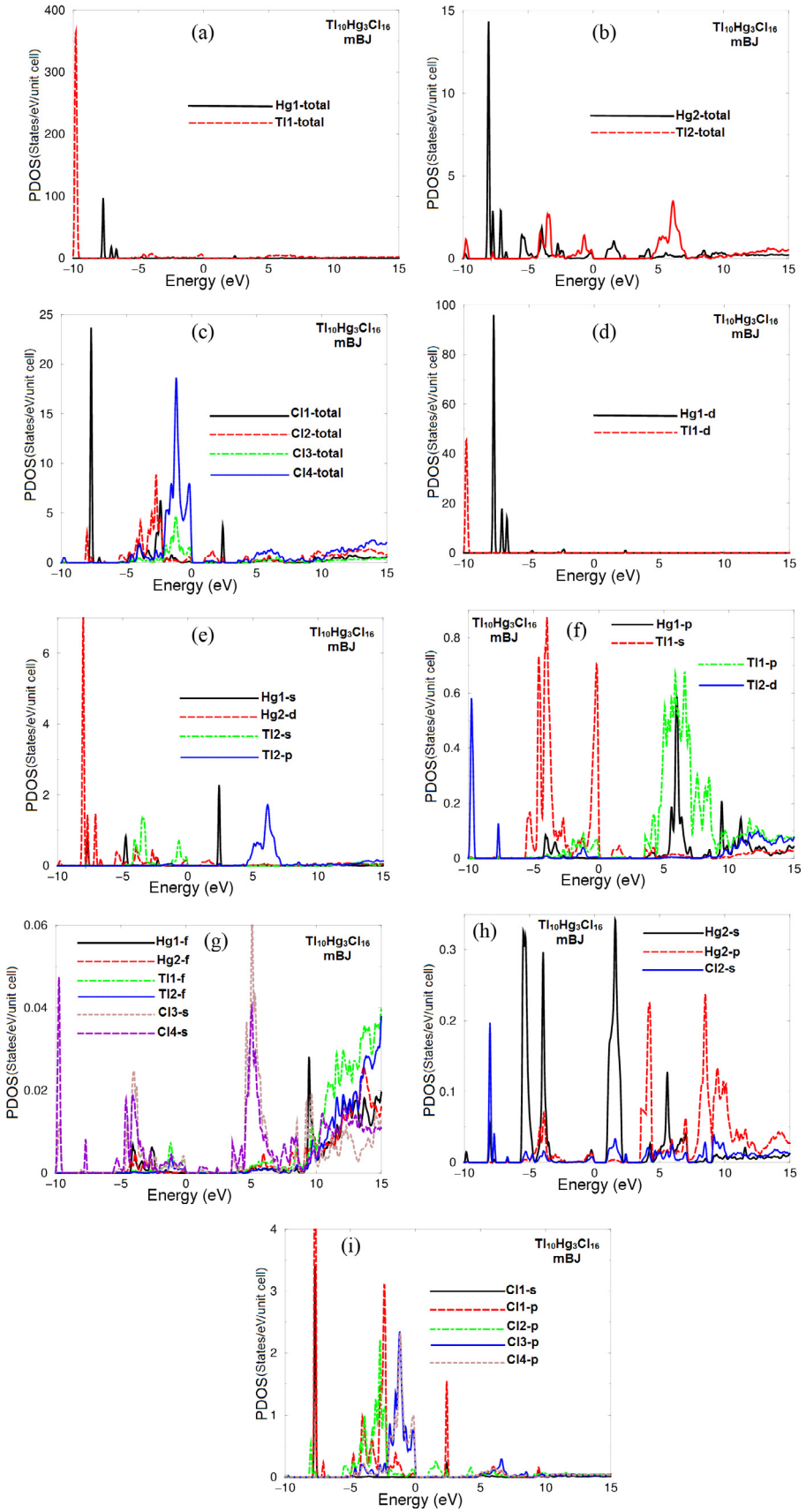

Fig. 3. The calculated partial density of states of $Tl_{10}Hg_3Cl_{16}$ single crystals: (a) the TDOS of Hg1 and Tl1 atoms, (b) the TDOS of Hg2 and Tl2 atoms, (c) the TDOS of Cl1, Cl2, Cl3, and Cl4 atoms, (d) the PDOS of Hg1-*d* and Tl1-*d* states, (e) the PDOS of Hg1-*s*, Hg2-*d*, and Tl2-*s*/*p* states, (f) the PDOS of Hg1-*p*, Tl1-*s*/*p*, and Tl2-*d* states, (g) the PDOS of Hg1-*f*, Hg2-*f*, Tl1-*f*, Tl2-*f*, Cl3-*s*, and Cl4-*s* states, (h) the PDOS of Hg2-*s*/*p* and Cl2-*s* states, (i) the PDOS of Cl1-*s*/*p*, Cl2-*p*, Cl3-*p*, and Cl4-*p* states.

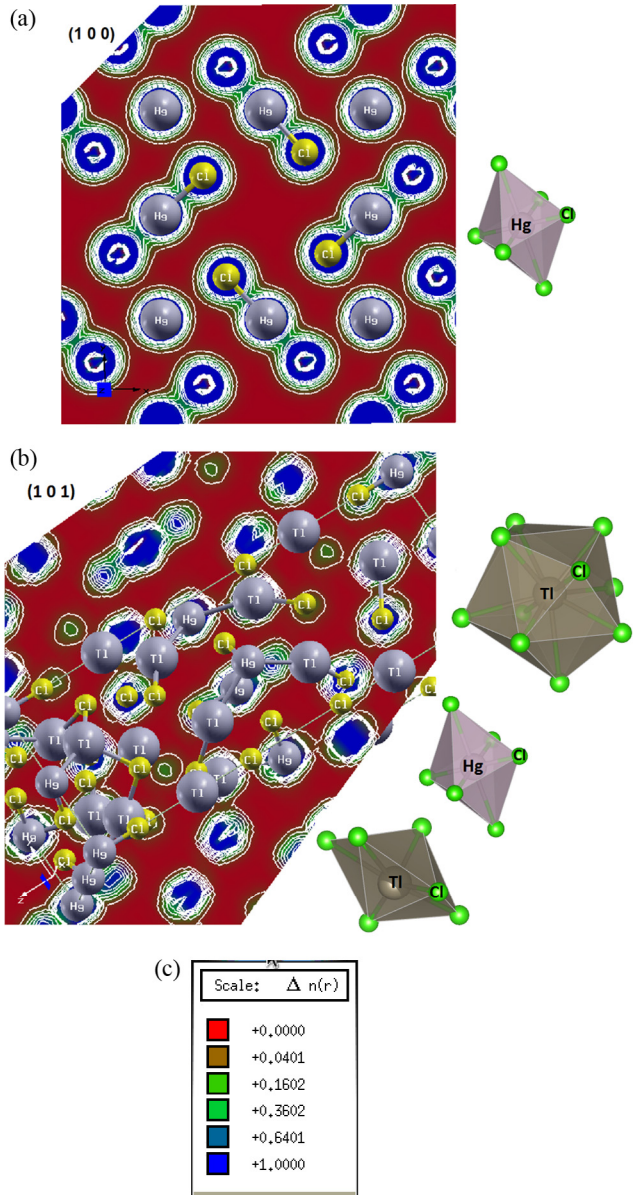

Fig. 4. Calculated electronic charge density distribution: (a) crystallographic plane (100), which shows that the Hg atoms have only tetrahedral surroundings, (b) crystallographic plane (101), which shows that the Hg atoms have only tetrahedral surroundings and the Tl atoms have octahedral and tetrahedral surroundings, (c) thermoscale.

Table 2
The calculated values of the ionic character.

Bonds	P (%)
Hg—Cl	13.85
Hg—Tl	6.58
Cl—Tl	32.94

Tl atoms. The calculated Hg—Cl bond lengths in the $HgCl_6$ octahedra are shorter than the Tl—Cl bond lengths in the $TlCl_{10}$ poyhedra and $TlCl_6$ octahedra (Table 2). The crystallographic planes show that a charge transfer toward Cl atoms occurs, as shown by the blue uniform spheres surrounded the Cl atoms, indicating the maximum charge accumulated according to the thermoscale (Fig. 4c) [69]. To provide a quantitative comparison between theoretical and experimental values of the bond lengths and angles, we have calculated the parameters for the $Tl_{10}Hg_3Cl_{16}$ crystal, as shown in Tables 3 and 4. It is clear that there is good agreement with the experimental data [2]. This reveals the accuracy of the method used here, and therefore we can conclude that our calculated energy band gap could be in close agreement with the expected experimental value. The bond lengths and the two crystallographic planes reveal that the $Tl_{10}Hg_3Cl_{16}$ single crystal possesses considerable anisotropy.

The photocatalytic oxidation of the materials is mainly attributed to the participation of superoxide radicals ($O_2^{\cdot-}$), hydroxyl radicals ($^{\cdot}OH$), and photogenerated holes [70] see Fig. 2a. To understand the photocatalytic mechanism of $Tl_{10}Hg_3Cl_{16}$, the reduction and oxidation potentials of the conduction band and the valence band edge at the point of zero charge can be calculated following the expressions given in Ref. [71],

$$E_{CB} = \chi - E^{C} - (E_g/2), \tag{2}$$

$$E_{VB} = E_{CB} + E_g, \tag{3}$$

where E_{CB} and E_{VB} are the potentials of the conduction band and the valence band edge, respectively, E^C is the free energy corresponding to the hydrogen scale, and the value is ~4.5 eV [71], and E_g and χ are the band gap and the electronegativity of semiconductors, respectively. χ is defined as the geometric mean of the absolute electronegativities of the constituent atoms. The absolute electronegativity of an individual atom is the arithmetic mean of the atomic electron affinity and the first ionization energy [71]. The E_{CB} and E_{VB} values of $Tl_{10}Hg_3Cl_{16}$ are 0.292 and 1.962 eV, respectively. It can be clearly seen that the CB edge potential is less than the VB potential, indicating that $Tl_{10}Hg_3Cl_{16}$ has a strong reduction power for H_2 production. Generally, an appropriate band gap width and suitable CB edge position together contribute to optimal H_2 production activity under light irradiation. Therefore, a balance between the light absorption capacity and the reduction power in the investigated material leads to higher efficiency of light-driven photocatalytic H_2 production.

3.3. Photophysical properties (linear optical response)

The tetragonal symmetry exhibits three nonzero components of the second-order dielectric (optical) tensor along the polarization directions [100], [010], and [001]. These correspond to the electric field $\vec{E}$ being directed along the **a**, **b**, and **c**rystallographic axes. Two of them along [100] and [010] are equal, and therefore, two tensor components completely define the linear optical response. The imaginary parts can be obtained using an expression taken from Ref. [72],

$$\varepsilon_2^{ij}(\omega)\frac{8\pi^2\hbar^2e^2}{m^2V}\sum_k\sum_{cv}(f_c - f_v)\frac{p_{cv}^i(k)p_{vc}^j(k)}{E_{vc}^2}\delta[E_c(k) - E_v(k) - \hbar\omega], \tag{4}$$

where m, e, and $\hbar$ are the electron mass and charge and Planck's constant, respectively. f_c and f_v represent the Fermi distributions of the conduction and valence bands, respectively. The term $p_{cv}^i(k)$ denotes the momentum matrix element transition from the energy level c of the conduction band to the level v of the valence band at a certain **k**-point in the BZ, and V is the unit cell volume.

The calculated imaginary part of the optical function's dispersion (Fig. 5a) shows pronounced structures of the nonzero major tensor components, $\varepsilon_2^{xx}(\omega)$ and $\varepsilon_2^{zz}(\omega)$. The absorption edge (threshold) of $\varepsilon_2^{xx}(\omega)$ and $\varepsilon_2^{zz}(\omega)$ is located at 0.97 eV. It has been noted that the $\varepsilon_2^{xx}(\omega)$ tensor component exhibits four main spectral features, which we denoted as E1, E2, E3, and E4, whereas the $\varepsilon_2^{zz}(\omega)$ exhibits

Table 3
Calculated bond lengths in comparison with the experimental ones [2,10].

Bonds	This work	Exp.	Bonds	This work	Exp.
Hg(1)—Cl(1)	2.311	2.360(3)[a]	Tl(1)—Cl(4)	3.400	3.404(14)[a]
Hg(1)—Cl(2)	3.001	3.098(17)[a]	Tl(1)—Cl(4)	3.616	3.639(15)[a]
Hg(2)—Cl(4)	2.413	2.451(5)[a]	Tl(1)—Cl(1)	3.402	3.416(4)[a]
Tl(1)—Tl(1)	2.667	3.681(4)[a]	Tl(1)—Cl(3)	3.002	3.055(5)[a]
Tl(1)—Cl(2)	3.009	3.106(14)[a]	Tl(2)—Cl(4)	3.611	3.625(15)[a]
Tl(1)—Tl(2)	3.463	3.470(16)[a]	Tl(2)—Cl(4)	3.421	3.432(13)[a]
Tl(1)—Cl(2)	3.337	3.349(14)[a]	Tl(2)—Cl(1)	3.722	3.760(3)[a]
Tl(1)—Cl(4)	3.201	3.216(15)[a]	Tl(2)—Cl(3)	3.298	3.300(4)[a]
C(11)—C(12)	4.379	4.382[b]	C(13)—C(14)	4.478	4.484[b]
C(11)—C(14)	4.520	4.528[b]	C(13)—C(12)	4.631	4.636[b]

Table 4
Calculated bond angles in comparison with the experimental one [2].

Bond angles	This work	Exp.
Cl(1)—Hg(1)—Cl(2)	90.0°	90.0°
Cl(1)—Hg(1)—Cl(1)	180.0°	180.0°
Cl(4)—Hg(2)—Cl(4)	112.0°	112.2°

five spectral features, E1, E2, E3, E4, and E5. In the energy regions 0.97–2.0 and 4.0–8.0 eV there exists considerable anisotropy between $\varepsilon_2^{xx}(\omega)$ and $\varepsilon_2^{zz}(\omega)$, which indicates that $Tl_{10}Hg_3Cl_{16}$ is a uniaxial crystal. The E1 and E2 spectral features belong to the optical transitions from Tl2-*s*, Tl1-*s*/*p*, Hg2-*d*, Cl3-*p*, Cl4-*p*, and Cl2-*p* valence bands to Hg2-*s*/*d*, Tl1-*s*, and Cl2-*s*/*p* conduction bands. The fundamental spectral structure, which is situated between 4.0 and 7.5 eV, consists of the spectral features E3 for both $\varepsilon_2^{xx}(\omega)$ and $\varepsilon_2^{zz}(\omega)$, and E4 for $\varepsilon_2^{zz}(\omega)$ are due to the transitions from Tl2-*s*, Hg2-*s*/*d*, Tl-1-*s*/*p*, Cl3-*p*, and Cl4-*p* valence bands to Hg2-*s*/*d*, Hg1-*s*, Tl-*p*, Cl1-*p*, Cl2-*p*, Cl3-*s*, and Cl4-*s* conduction bands. The tail (E5 for $\varepsilon_2^{zz}(\omega)$ and E4 for $\varepsilon_2^{xx}(\omega)$) comes from the optical transitions between Hg1-*d*, Hg2-*d*, Tl1-*s*/*d*, Tl-2-*s*, and Cl1-*s*/*p* valence bands and Tl2-*p*/*d*/*f*, Tl1-*p*, Hg1-*p*/*f*, Hg2-*s*/*f*, Tl1-*f*, Cl2-*s*, Cl3-*s*, and Cl4-*s* conduction bands.

By means of the Kramers–Kronig transformation [73], we can derive the real part of the corresponding principal complex tensor

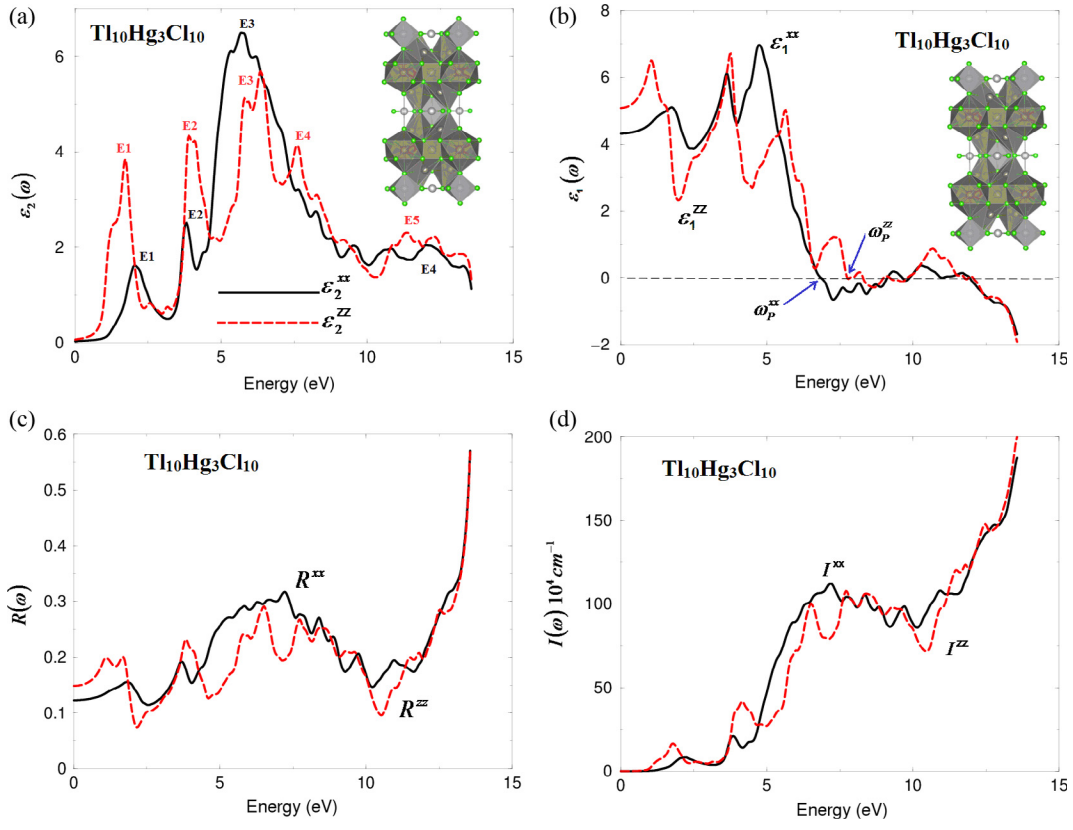

Fig. 5. (a) Calculated $\varepsilon_2^{xx}(\omega)$ (dark solid curve-black color online), $\varepsilon_2^{zz}(\omega)$ (light long dashed curve, red color online), (b) calculated $\varepsilon_1^{xx}(\omega)$ (dark solid curve, black color online), $\varepsilon_1^{zz}(\omega)$ (light long dashed curve, red color online), (c) calculated $R^{xx}(\omega)$ (dark solid curve, black color online), $R^{zz}(\omega)$ (light long dashed curve, red color online), (d) calculated $I^{xx}(\omega)$ (dark solid curve, black color online), $I^{zz}(\omega)$ (light long dashed curve, red color online). (e) The optical band gap value of the semiconductor materials can be solved as follows: The square of absorption coefficient $I(\omega)$ is linear with energy (E) for direct optical transitions in the absorption edge region, whereas the square root of $I(\omega)$ is linear with E for indirect optical transitions. The calculated electronic band structure confirms the direct nature of the band gap of $Tl_{10}Hg_3Cl_{16}$. It is clearly shown that the square of $I(\omega)$ versus E is linear in the absorption edge region. This plot suggests that the absorption edge of $Tl_{10}Hg_3Cl_{16}$ is caused by direct transitions. We can conclude that the absorption edge of $Tl_{10}Hg_3Cl_{16}$ occurs at λ = 742.3 nm, and the optical band gap is estimated to be 1.67 eV. (f) Calculated $L^{xx}(\omega)$ (dark solid curve, black color online), $L^{zz}(\omega)$ (light long dashed curve, red color online), (g) calculated $n^{xx}(\omega)$ (dark solid curve, black color online), $n^{zz}(\omega)$ (light long dashed curve, red color online), (h) calculated birefringence $\Delta n(\omega)$ of $Tl_{10}Hg_3Cl_{16}$ single crystal. (For interpretation of the references to colour in this figure legend, the reader is referred to the web version of this article.)

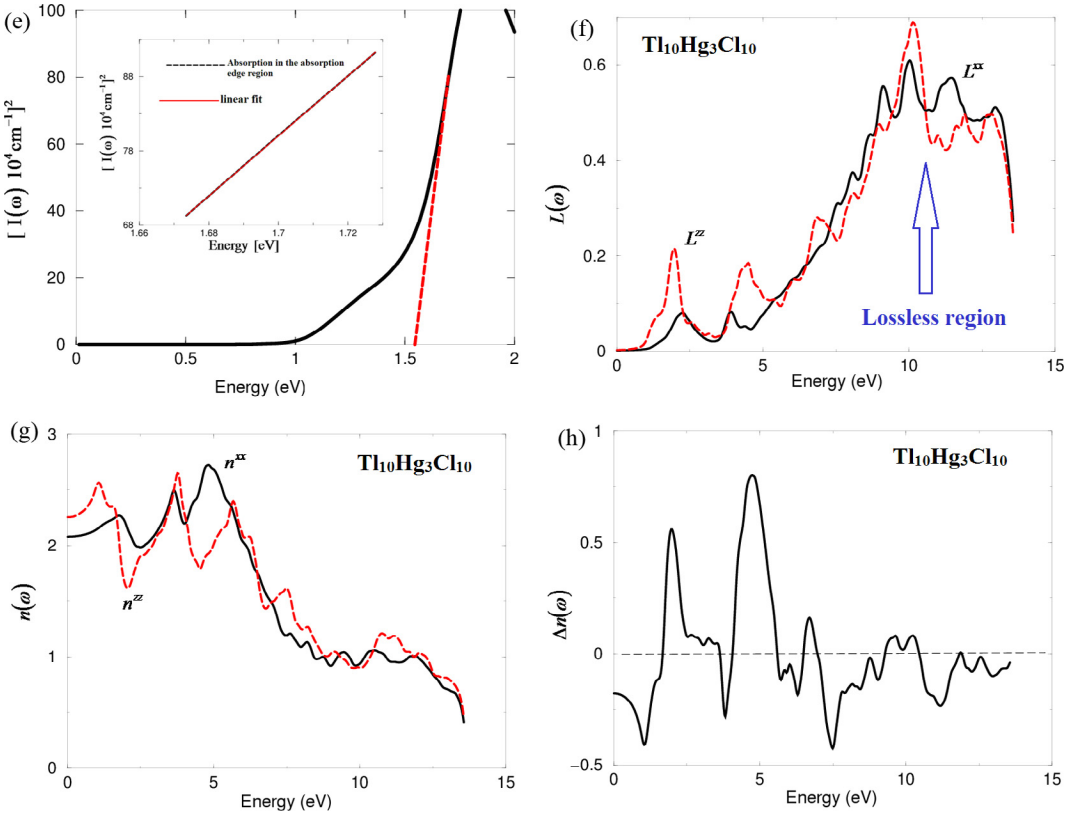

Fig. 5 (*continued*)

components from the existing information about the imaginary part. The obtained real part $\varepsilon_1^{xx}(\omega)$ and $\varepsilon_1^{zz}(\omega)$ is shown in Fig. 5b. The vanishing frequency value of the dielectric function that defines the static electronic dielectric constant $\varepsilon_\infty = \varepsilon_1(\omega = 0)$ can be obtained from $\varepsilon_1^{xx}(0)$ and $\varepsilon_1^{zz}(0)$, as shown in Table 2. With the aid of these values, we can estimate the value of the optical gap following the Penn model [74]. Also, the uniaxial anisotropy ($\delta\varepsilon$) shows that this crystal possesses positive uniaxial anisotropy (Table 5). Furthermore, the plasmon oscillations ω_p^{xx} and ω_p^{zz}, which are associated with the existence of plasma oscillations (plasmons), can be obtained at the energies where $\varepsilon_1^{xx}(\omega)$ and $\varepsilon_1^{zz}(\omega)$ cross zero. These values are given in Table 5.

From the existing information on the imaginary and real parts of the optical function's dispersion, we can calculate the reflectivity spectra $R(\omega)$, refractive indices $n(\omega)$, loss functions $L(\omega)$, and absorption coefficient $I(\omega)$. The reflectivity spectra along the [100] and [001] polarization directions are represented in Fig. 5c. In the low-energy region (0.0–5.0 eV), both $R^{xx}(\omega)$ and $R^{zz}(\omega)$ spectral components exhibit low reflectivity <20.0% as average it is clear that $R^{zz}(\omega)$ behaves as the dominant component with reflectivity about 20.0%. The reflectivity spectra of the two spectral components vary along the energy scale to reach a maximum value (57.0%) at around 13.5 eV, which results from the transitions of *s*-states of valence bands to *p*-states of conduction bands. The first reflectivity maximum (~34.0%) occurs at around ~7.5 eV, followed by the first reflectivity minimum, which is situated at around ~11.0 eV, confirming the occurrence of collective plasmon resonance. The first reflectivity maximum and minimum occur according to the transition from *p*-states of Cl and Tl atoms (valence bands) to *s*-states of Hg and Cl atoms (conduction bands).

Table 5
The calculated $\varepsilon_1^{xx}(0)$, $\varepsilon_1^{zz}(0)$, $\delta\varepsilon$, ω_p^{xx}, ω_p^{zz}, $n^{xx}(0)$, $n^{zz}(0)$, and $\Delta n(0)$.

Component	This work
$\varepsilon_1^{xx}(0)$	4.319
$\varepsilon_1^{zz}(0)$	5.086
$\varepsilon_1^{average}(0)$	4.702
$\delta\varepsilon$	0.163
ω_p^{xx}	6.870
ω_p^{zz}	7.768
$n^{xx}(0)$	2.078
$n^{zz}(0)$	2.255
$\Delta n(0)$	0.177

The calculated absorption coefficient $I(\omega)$ of the two spectral components is illustrated in Fig. 5d. The calculated absorption coefficient shows the fundamental optical absorption edge at around 0.97 eV, and then the absorption coefficient increases drastically up to a maximum value at around 13.5 eV. It is clear that the $Tl_{10}Hg_3Cl_{16}$ single crystal exhibited a wide optical transparency region. The absorption coefficient spectra consist of low-absorption and high-absorption regions. The optical band gap values of the semiconductor materials can be solved as follows: the square of the absorption coefficient $I(\omega)$ is linear with energy (E) for direct optical transitions in the absorption edge region, whereas the square root of $I(\omega)$ is linear with E for indirect optical transitions [56,57]. Since the calculated electronic band structure confirms the direct nature of the band gap of $Tl_{10}Hg_3Cl_{16}$, the data plots of the square of $I(\omega)$ versus E are shown in Fig. 5e. It is clearly shown that the square of $I(\omega)$ versus E is linear in the absorption edge region. This plot suggests that the absorption edge of $Tl_{10}Hg_3Cl_{16}$ is caused by direct transitions. Following Fig. 5e, we can conclude that the absorption edge of $Tl_{10}Hg_3Cl_{16}$ occurs at λ = 742.3 nm, and the optical band gap is estimated to be 1.67 eV. The narrow optical band gap of photocatalyst material not only benefits the absorption of more photons from sunlight, but also promotes the excitation of photogenerated electrons from

the VB to the CB, which makes the photocatalyst capable of visible-light H_2-production activity. In addition to the effect of the optical band gap value, the CB edge position of the photocatalyst material is another important factor for effective photocatalytic H_2 production [75]. For photocatalytic water splitting, the optical band gap of the photocatalyst material must be sufficiently large to overcome the endothermic character of the water-splitting reaction, i.e., wider than 1.23 eV [76] therefore, $Tl_{10}Hg_3Cl_{16}$ (E_g = 1.67 eV) is expected to be an active photocatalyst. The other important factor for a photocatalyst is the range of light absorbed (see Fig. 4e). The optical absorption induces the transfer of *e* from the VB to the CB, generating the *e*–*h* pairs, which can thence migrate to the surface to participate in oxidation and reduction reactions, respectively [77,78]. Usually, the locations of the VBM and the CBM determine the oxidation and reduction capabilities of photogenerated holes and electrons, respectively [77]. The reduction potential level of the electron-accepters should be energetically below the CBM, whereas the oxidization potential level of the electron-donors should be above the VBM [79].

The loss function's peaks are initiated at the values of the plasma frequencies ω_p^{xx} and ω_p^{zz} (Fig. 5f). These peaks represent the negative parts of $\varepsilon_1^{xx}(\omega)$ and $\varepsilon_1^{zz}(\omega)$. The calculated refractive indices, as shown in Fig. 5g, confirm the existence of considerable anisotropy, and from $n(0)$ we can estimate the value of the optical band gap ($n = \sqrt{\varepsilon}$). Furthermore, the values of the birefringence $\Delta n(\omega)$ can be obtained from $n^{xx}(\omega)$ and $n^{zz}(\omega)$, as shown in Fig. 5h and Table 5.

3.4. Transport properties

To understand the photocatalytic mechanism in $Tl_{10}Hg_3Cl_{16}$, we have investigated the influence of the temperature on the carrier concentration (n) of $Tl_{10}Hg_3Cl_{16}$ at a certain value of the chemical potential ($\mu = E_F$). It has been found that n increases almost linearly with increasing T, as illustrated in Fig. 6a, and the positive sign indicates that the $Tl_{10}Hg_3Cl_{16}$ exhibits p-type conductions. To support this statement, we have investigated the n in the vicinity of E_F at three T values, as shown in Fig. 6b. It has been noticed

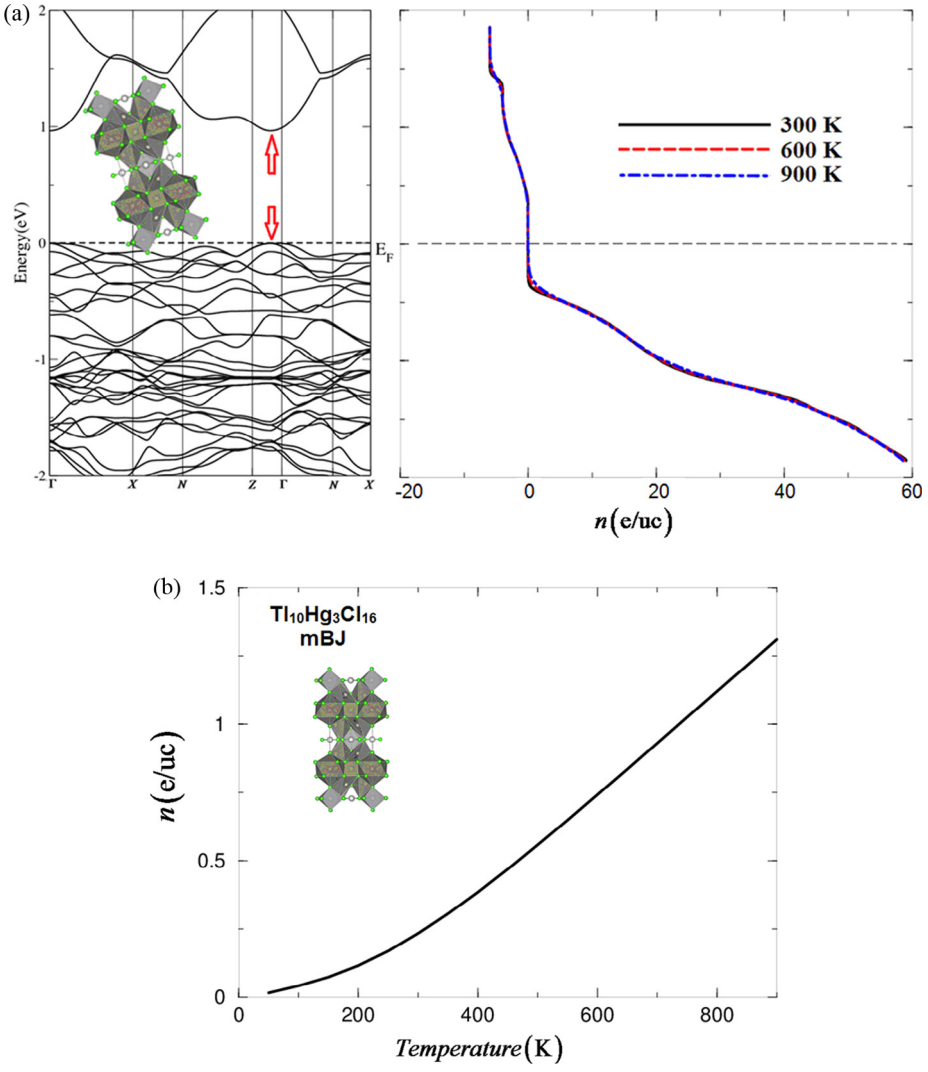

Fig. 6. (a) The temperature-induced carrier concentration of $Tl_{10}Hg_3Cl_{16}$ single crystals per unit cell (e/uc) versus temperature, (b) calculated carrier concentration as a function of chemical potential ($\mu - E_F = \pm 0.2$ eV) at three constant temperatures (300, 600, and 900 K), (c) the electrical conductivity versus the temperature, (d) the electrical conductivity as a function of chemical potential ($\mu - E_F = \pm 0.2$ eV) at three constant temperatures (300, 600, and 900 K), (e) the electronic thermal conductivity versus the temperature, (f) the electronic thermal conductivity as a function of chemical potential ($\mu - E_F = \pm 0.2$ eV) at three constant temperatures (300, 600, and 900 K), (g) the Seebeck coefficient versus the temperature (h) the Seebeck coefficient as a function of chemical potential ($\mu - E_F = \pm 0.2$ eV) at three constant temperatures (300, 600, and 900 K), (i) the power factor versus the temperature, (j) the power factor as a function of the chemical potential ($\mu - E_F = \pm 0.2$ eV) at three constant temperatures (300, 600, and 900 K).

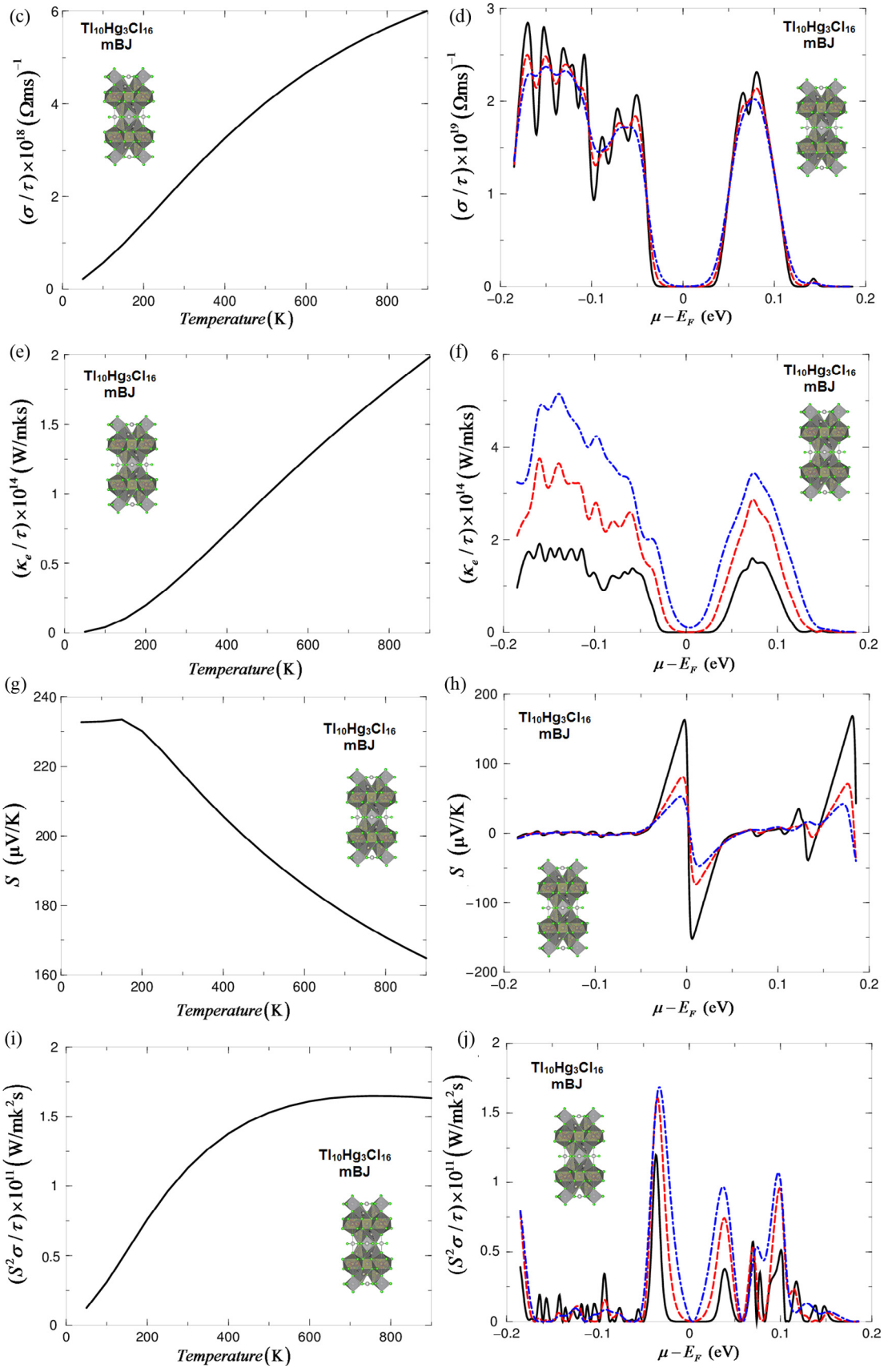

Fig. 6 (*continued*)

that the difference between chemical potential and Fermi energy ($\mu - E_F$) is positive for valence bands and negative for conduction bands. It has been found that $Tl_{10}Hg_3Cl_{16}$ exhibits a maximal n in the vicinity of E_F.

It is well known that the temperature difference between the two ends of a material is responsible for producing thermoelectric voltage. To achieve high thermoelectric efficiency, it is necessary that the material possess high σ/τ, high S, and low k/τ [80]. Therefore, to show the high σ/τ, high-mobility carriers is required. To achieve this, a material with small effective mass is needed. It has been noticed from the electronic band structure (Fig. 2) that the high k-dispersion bands around Fermi level (E_F) possess low effect masses and, hence, high-mobility carriers (Table 6), which favor the charge transfer process the effective mass provides essential information to see the photocatalytic mechanism. The mobility of the photogenerated carriers significantly influences the photocatalytic efficiency [81,82] and the higher photogenerated carrier mobility enhances the photocatalytic performance [83]. Moreover, the great effective mass difference ($D = m_e^*/m_h^*$) between electron (e) and hole (h) (Table 6) can facilitate e and h migration and separation, and finally improve the photocatalytic performance. The effective mass of e is greater than that of the h, resulting in a significant difference in the mobility between e and h. The mobility of photoexcited carriers can be indirectly assessed by their effective mass ($\eta_e = e\tau_e/m_e^*$ and $\eta_h = e\tau_h/m_h^*$). Here we call the mobility η to distinguish between the mobility and the chemical potential (μ). The large mobility difference is useful for the separation of e and h, reduction of e and h recombination rate, and improvement of the photocatalytic activity. It is clear from Table 5 that the effective masses of the e and h are small, and thus, we can deduce that the photogenerated carrier transfer can be fast along different directions.

To ascertain that $Tl_{10}Hg_3Cl_{16}$ is expected to give maximum efficiency at E_F, we have investigated σ/τ as a function of T at a certain value of chemical potential, as shown in Fig. 6c, which represents the temperature variation of the σ/τ. It is clear that σ/τ increases with T to reach its maximum value of about 6.0×10^{18} $(\Omega\,ms)^{-1}$ at 900 K. It is clear that σ/τ shows slight deviation from linear temperature dependence. Therefore, at a certain chemical potential, n and σ/τ are temperature-dependent. In addition to this, we have calculated σ/τ as a function of chemical potential at three constant temperatures (300, 600, and 900 K), as shown in Fig. 6d. It is clear that above E_F, a significant increase in σ/τ occurs to reach a maximum value of about 2.343×10^{19} $(\Omega\,ms)^{-1}$ at $\mu - E_F$ = +0.1 eV, while below E_F it is about 2.859×10^{19} $(\Omega\,ms)^{-1}$ at $\mu - E_F$ = −0.18 eV. It is clear that the temperature has an insignificant influence on σ/τ in the chemical potential ($\mu - E_F$) range between −0.2 and +0.2 eV.

The thermal conductivity (k) has two parts the electronic contribution k_e (electrons and holes transporting heat) and the phonon contribution k_l (phonons traveling through the lattice). BoltzTraP code calculates only the electronic part k_e [41]. We have calculated k_e/τ of $Tl_{10}Hg_3Cl_{16}$ as a function of T at Fermi level (a certain chemical potential value $\mu = E_F$), as shown in Fig. 6e, which represents the T variation of the k_e/τ. It is clear that k_e/τ increases lineally with increasing T. The results show that k_e/τ is temperature-dependent. In addition to that, we have calculated k_e/τ as a function of chemical potential at three constant temperatures, as shown in Fig. 6f. It is clear that a significant increase in k_e/τ occurs with increasing T, and the temperature 900 K induced the highest k_e/τ values, while 300 K induced the lowest k_e/τ values, confirming that 300 K is the optimal temperature that gives the lowest k_e/τ values in the chemical potential range $\mu - E_F$ = ±0.2 eV.

The very important quantity that is related to the electronic band structure of the materials is the Seebeck coefficient (S). Thus, we have calculated S as a function of T at a certain value of chemical potential, as shown in Fig. 6g. At low T < 200 K, the Seebeck coefficient exhibits its highest value of about 233 μV/K and then it drops to the lower value with increasing T. Further, we have calculated S as a function of chemical potential at three constant temperatures (Fig. 6h). One can see in the vicinity of E_F the S exhibits pronounced structures at E_F, and above E_F. In the vicinity of E_F, S exhibits two pronounced structures just below and above E_F, with the highest value of S at 300 K (180 and −180 μV/K) and +180 μV/K at $\mu - E_F$ = +0.18 eV. From Fig. 6h, it is clear that the obtained values of S are negative/positive for the entire range of the chemical potential, suggesting the presence of n/p-type charge carriers. The sign of S indicates the type of dominant charge carriers: S with positive sign represent the p-type materials, whereas n-type materials have negative S [41,84–86].

One can see that the power factor, defined as $P = S^2\sigma/\tau$, is directly proportional to S^2 and σ/τ. Therefore, to gain high P, one need to maintain the values of S^2 and σ/τ. It is well known that figure of merit is a very important quantity for calculating the transport properties of the materials. The dimensionless figure of merit is written as ($ZT = S^2\sigma T/k_e + k_l$) [87,88], which shows that P comes in the numerator of the figure of merit thus P is an important quantity and play a principal role in evaluating the transport properties of the materials.

We have investigated the influence of T variation on P (Fig. 6i), and it is clear that, in a T range between 50 and 500 K, P increases linearly with T. Above 500 K, P reaches the saturated value. Furthermore, to ascertain the influence of varying the chemical potential on P, we have calculated P at three fixed temperatures as a function of chemical potential, as shown in Fig. 6j. It has been found that $Tl_{10}Hg_3Cl_{16}$ exhibits the highest P just below E_F. It is interesting to see that increasing the temperature causes significant increases in P. The increase of the Seebeck coefficient also leads to a maximum of P at the vicinity of E_F, it is slightly shifted compared with the maximum of the Seebeck coefficient due to the decreasing conductivity.

We would like to mention here that, in our previous works [89–92], we have calculated the transport properties using the FPLAPW method within BoltzTraP code for several systems whose transport properties are known experimentally, and very good agreement with the experimental data was obtained. Thus, we believe that our calculations reported in this paper would produce very accurate and reliable results.

Table 6
Calculated effective masses.

Effective mass	Value
m_e^*/m_o	0.01854
m_{hh}^*/m_o	0.07091
m_{lh}^*/m_o	0.02487
$D = m_{hh}^*/m_e^*$	3.82470
$D = m_e^*/m_{hh}^*$	0.26145
$D = m_{lh}^*/m_e^*$	1.34142
$D = m_e^*/m_{lh}^*$	0.74547

4. Conclusions

The full potential method within the generalized gradient approximation (PBE-GGA) was used to optimize the experimental structural geometry of $Tl_{10}Hg_3Cl_{16}$ compound. Three types of exchange correlation potentials, namely LDA, PBE-GGA, and mBJ are used to perform the calculations of the electronic band structure, density of states, electronic charge density distribution, and optical and transport properties. Calculations show that an energy

band gap of about 0.82, 0.88, and 0.97 eV is obtained using LDA, PBE-GGA, and mBJ, respectively. These values are much higher than 0.22 eV, which is obtained from previous calculations using the full-potential linear muffin-tin orbital (FP-LMTO) method within LDA therefore, we expected our obtained results are more accurate based on our experiences on using mBJ. We would like to mention here that in our previous work we have used mBJ to calculate the energy band gap of several systems whose energy band gaps are known experimentally. In those previous calculations, we found very good agreement with the experimental data. Thus, we believe that our calculations reported in this paper would produce very accurate and reliable results. The calculated density of states reveals the orbitals that form the conduction band minimum, the valence band maximum, and the existence of hybridization. In order to understand the bonding feature, we have calculated the valence charge density distributions, which show that there exist ionic and covalent bonding. The obtained optical properties help to uncover the electronic structure, and the calculated transport properties reveal that the investigated compound could be an attractive candidate for use in clean energy.

Acknowledgments

The result was developed within the CENTEM project, reg. no. CZ.1.05/2.1.00/03.0088, co-funded by the ERDF as part of the Ministry of Education, Youth and Sports OP RDI program and, in the follow-up sustainability stage, supported through CENTEM PLUS (LO1402) by financial means from the Ministry of Education, Youth and Sports under National Sustainability Programme I. Computational resources were provided by the MetaCentrum (LM2010005) and CERIT-SC (CZ.1.05/3.2.00/08.0144) infrastructures.

References

[1] https://www.researchgate.net/publication/228413833_A_systematic_search_for_new_scintillators_using_electronic_structure_calculations.
[2] K. Brodersen, K.P. Jensen, G. Thiele, Z. Naturforsch. B 35 (1980) 259–264.
[3] D. Kahler, N.B. Singh, D.J. Knuteson, B. Wagner, A. Berghmans, S. McLaughlin, M. King, K. Schwartz, D. Suhre, M. Gotlieb, Nucl. Instrum. Methods Phys. Res. A 652 (2011) 183–185.
[4] M. Sarfaraz Nawaz, Rafiuddin, Ionics 13 (2007) 35–40.
[5] D.S. Kalyagin, Yu.E. Ermolenko, Yu.G. Vlasov, Russ. J. Appl. Chem. 81 (2008) 2172–2174.
[6] Yu.E. Ermolenko, D.S. Kalyagin, S.N. Subbotina, V.V. Kolodnikov, Yu.G. Vlasov, Russ. J. Appl. Chem. 86 (2013) 192–199.
[7] V.A. Franiv, O.V. Bovgyra, I.S. Girnyk, O.S. Kushnir, O.V. Futey, A.P. Vas'kiv, Electron. Inf. Technol. 3 (2013) 34–39.
[8] K. Brodersen, G. Thiele, G. Görz, Z. Anorg, Allg. Chem. 401 (1973) 217–226.
[9] K. Brodersen, K.P. Jensen, D. Messer, G. Thiele, H.J. Berthold, D. Haas u. R. Tamme, Z. Anorg. Allg. Chem. 456 (1979) 29.
[10] O.Y. Khyzhun, M. Piasecki, I.V. Kityk, I. Luzhnyi, A.O. Fedorchuk, P.M. Fochuk, S. I. Levkovets, M.V. Karpets, O.V. Parasyuk, J. Solid State Chem. 242 (2016) 193–198.
[11] N.M. Denysyuk, V.L. Bekenev, M.V. Karpets, O.V. Parasyuk, S.P. Danylchuk, O.Y. Khyzhun, J. Alloys Compd. 576 (2013) 271–278.
[12] O.Y. Khyzhun, V.L. Bekenev, N.M. Denysyuk, O.V. Parasyuk, A.O. Fedorchuk, J. Alloys Compd. 582 (2014) 802–809.
[13] A.A. Lavrentyev, B.V. Gabrelian, V.T. Vu, P.N. Shkumat, G.L. Myronchuk, M. Khvyshchun, A.O. Fedorchuk, O.V. Parasyuk, O.Y. Khyzhun, Opt. Mater. 42 (2015) 351–360.
[14] Zhongli Li, Xiaoping Chen, Wenfeng Shangguan, Yanjie Su, Yijian Liu, Xinwei Dong, Poonam Sharma, Yafei Zhang, Int. J. Hydrogen Energy. http://dx.doi.org/10.1016/j.ijhydene.2016.12.047.
[15] S.U.M. Khan, M. Al-Shahry, W.B. Ingler, Science 297 (2002) 2243–2244.
[16] A. Kudo, Y. Miseki, Chem. Soc. Rev. 38 (253e) (2009) 78.
[17] X.B. Chen, S.H. Shen, L.J. Guo, S.S. Mao, Chem. Rev. 110 (2010) 6503–6570.
[18] H.B. Yi, T.Y. Peng, D.N. Ke, D. Ke, L. Zan, C.H. Yan, Int. J. Hydrogen Energy 33 (2008) 672–678.
[19] C.C. Hu, H. Teng, J. Catal. 272 (2010) 1–8.
[20] K.E. Dekrafft, C. Wang, W.B. Lin, Adv. Mater. 24 (2012) 2014–2018.
[21] N.Z. Bao, L.M. Shen, T. Takata, K. Domen, Chem. Mater. 20 (2008) 110–117.
[22] M. Matsumura, S. Furukawa, Y. Saho, H. Tsubomura, J. Phys. Chem. 89 (1985) 1327–1329.
[23] S.W. Liu, J.G. Yu, M. Jaroniec, J. Am. Chem. Soc. 132 (2010) 11914–11916.
[24] J.R. Ran, J.G. Yu, M. Jaroniec, Green Chem. 13 (2011) 2708–2713.
[25] H. Wang, W. Chu, H. Jin, Comput. Mater. Sci. 60 (2012) 224.
[26] K.P. Ong, D.J. Singh, P. Wu, Phys. Rev. B 83 (2011) 115110.
[27] D. Parker, D.J. Singh, Phys. Rev. B 83 (2011) 233206.
[28] D. Parker, M. Du, D.J. Singh, Phys. Rev. B 83 (2011) 245111.
[29] D.J. Singh, Phys. Rev. B 81 (2010) 195217.
[30] K.P. Ong, D.J. Singh, P. Wu, Phys. Rev. Lett. 104 (2010) 176601.
[31] G.B. Wilson-Short, D.J. Singh, M. Fornari, M. Suewattana, Phys. Rev. B 75 (2007) 035121.
[32] D.J. Singh, D. Kasinathan, J. Electron. Mater. 36 (2007) 736.
[33] D.J. Singh, Phys. Rev. B 76 (2007) 085110.
[34] D.J. Singh, Oxide Thermoelectrics, MRS Symp. Proc. 1044 (2008) U02–05.
[35] D.J. Singh, Alkaline earth filled nickel skutterudite antimonide thermoelectrics U.S. Patent 8,487,178, 2013.
[36] H.A.R. Aliabad, M. Ghazanfari, I. Ahmad, M.A. Saeed, Comput. Mater. Sci. 65 (2012) 509.
[37] P. Blaha, K. Schwarz, G.K.H. Madsen, D. Kvasnicka, J. Luitz, WIEN2k, An augmented plane wave plus local orbitals program for calculating crystal properties, Vienna University of Technology, Austria, 2001.
[38] W. Kohn, L.J. Sham, Phys. Rev. A 140 (1965) 1133.
[39] J.P. Perdew, S. Burke, M. Ernzerhof, Phys. Rev. Lett. 77 (1996) 3865.
[40] Fabien Tran, Peter Blaha, Phys. Rev. Lett. 102 (2009) 226401.
[41] G.K.H. Madsen, D.J. Singh, Comput. Phys. Commun. 175 (2006) 67–71.
[42] P.B. Allen, in: Quantum Theory of Real Materials, J.R. Chelikowsky, S.G. Louie, Kluwer, Boston, 1996, pp. 219–250.
[43] J.M. Ziman, Electrons and Phonons, Clarendon, Oxford, 2001.
[44] C.M. Hurd, The Hall Effect in Metals and Alloys, Plenum, New York, 1972.
[45] M.I. Kolinko, I.V. Kityk, A.S. Krochuk, J. Phys. Chem. Solids 53 (1992) 1315–1320.
[46] G.E. Davydyuk, O.Y. Khyzhun, A.H. Reshak, H. Kamarudin, G.L. Myronchuk, S.P. Danylchuk, A.O. Fedorchuk, L.V. Piskach, M.Yu. Mozolyuk, O.V. Parasyuk, Phys. Chem. Chem. Phys. 15 (2013) 6965.
[47] A.H. Reshak, Phys. Chem. Chem. Phys. 16 (2014) 10558.
[48] A.H. Reshak, Y.M. Kogut, A.O. Fedorchuk, O.V. Zamuruyeva, G.L. Myronchuk, O. V. Parasyuk, H. Kamarudin, S. Auluck, K.L. Plucinskig, J. Bila, Phys. Chem. Chem. Phys. 15 (2013) 18979.
[49] A.H. Reshak, D. Stys, S. Auluck, I.V. Kityk, Phys. Chem. Chem. Phys. 13 (2011) 2945.
[50] V.V. Atuchin, T.A. Gavrilova, J.-C. Grivel, V.G. Kesler, Surf. Sci. 602 (2008) 3095–3099.
[51] V.V. Atuchin, T.A. Gavrilova, J.-C. Grivel, V.G. Kesler, J. Phys. D Appl. Phys. 42 (2009) 035305.
[52] O.Y. Khyzhun, V.L. Bekenev, V.V. Atuchin, E.N. Galashov, V.N. Shlegel, Mater. Chem. Phys. 140 (2013) 558–595.
[53] V.V. Atuchin, E.N. Galashov, O.Y. Khyzhun, V.L. Bekenev, L.D. Pokrovsky, Yu.A. Borovlev, V.N. Zhdankov, J. Solid State Chem. 236 (2016) 24–31.
[54] K. Nouneh, Ali H. Reshak, S. Auluck, I.V. Kityk, R. Viennois, S. Benet, S. Charar, J. Alloys Compd. 437 (2007) 39–46.
[55] A.H. Reshak, K. Nouneh, I.V. Kityk, Jiri Bila, S. Auluck, H. Kamarudin, Z. Sekkat, Int. J. Electrochem. Sci. 9 (2014) 955–974.
[56] H. Huang, Y. He, X. Li, M. Li, C. Zeng, F. Dong, X. Du, T. Zhangd, Y. Zhang, J. Mater. Chem. A 3 (2015) 24547–24556.
[57] H. Huang, Y. He, Z. Lin, L. Kang, Y. Zhang, J. Phys. Chem. C 117 (2013) 22986–22994.
[58] J. Zhang, W. Yu, J. Liu, B. Liud, Appl. Surf. Sci. 358 (2015) 457–462.
[59] X. Li, J. Zhao, J. Yang, Sci. Rep. 3 (2013) 1858.
[60] Dong Won Hwang, Jae Sung Lee, Wei Li, Se Hyuk Oh, J. Phys. Chem. B 107 (21) (2003) 4963–4970.
[61] Hongwei Huang, Xiaowei Li, Jinjian Wang, Fan Dong, Paul K. Chu, Tierui Zhang, Yihe Zhang, ACS Catal. 5 (7) (2015) 4094–4103.
[62] Hongwei Huang, Xu Han, Xiaowei Li, Shichao Wang, Paul K. Chu, Yihe Zhang, ACS Appl. Mater. Interfaces 7 (2015) 482–492.
[63] P. Zhou, J.H. Wu, W.L. Yu, G.H. Zhao, G.J. Fang, S.W. Cao, Appl. Surf. Sci. 319 (2014) 167–172.
[64] P. Dufek, P. Blaha, K. Schwarz, Phys. Rev. B 50 (1994) 7279.
[65] V.L. Bekenev, O.Yu. Khyzhun, A.K. Sinelnichenko, V.V. Atuchin, O.V. Parasyuk, O.M. Yurchenko, Yu. Bezsmolnyy, A.V. Kityk, J. Szkutnik, S. Całus, J. Phys. Chem. Solids 72 (2011) 705–713.
[66] Anatoliy A. Lavrentyev, Boris V. Gabrelian, Tuan V. Vu, Peter N. Shkumat, Petro M. Fochuk, Oleg V. Parasyuk, Iwan V. Kityk, Ivan V. Luzhnyi, Oleg Y. Khyzhun, Michal Piasecki, Inorg. Chem. 55 (20) (2016) 10547–10557.
[67] A.A. Lavrentyev, B.V. Gabrelian, V.T. Vu, O.V. Parasyuk, A.O. Fedorchuk, O.Y. Khyzhun, Opt. Mater. 60 (2016) 169–180.
[68] Schlusseltechnologien Key Technologies, 41st IFF Springschool, 2010, pp A1–18.
[69] Chengyin Liu, Yihe Zhang, Fan Dong, A.H. Reshak, Liqun Ye, Nicola Pinna, Chao Zeng, Tierui Zhang, Hongwei Huang, Appl. Catal. B Environ. 203 (2017) 465–474.
[70] P.J. Zhou, G. Yu, M. Jaroniec, Adv. Mater. 26 (2014) 4920–4935.
[71] Q. Li, H. Meng, P. Zhou, Y.Q. Zheng, J. Wang, J.G. Yu, J.R. Gong, ACS Catal. 3 (2013) 882–889.
[72] F. Bassani, G. P. Parravicini, Electronic States and Optical Transitions in Solids Pergamon Press Ltd., Oxford, 1975, pp. 149–154.
[73] H. Tributsch, Z. Naturforsch. A 32A (1977) 972.
[74] D.R. Penn, Phys. Rev. B 128 (1962) 2093.
[75] Qin. Li, Huan Meng, Peng Zhou, Yingqiu Zheng, Juan Wang, Jiaguo Yu, JianRu Gong, Zn1−xCdxS solid solutions with controlled bandgap and enhanced visible-light photocatalytic H2-production activity, ACS Catal. 3 (2013) 882–889.

[76] X.C. Wang et al., A metal-free polymeric photocatalyst for hydrogen production from water under visible light, Nat. Mater. 8 (2009) 76–80.
[77] Jinfeng Zhang, Weilai Yu, Jianjun Liu, Baoshun Liu, Appl. Surf. Sci. 358 (2015) 457–462.
[78] J.C. Wu, J.W. Zheng, P. Wu, R. Xu, J. Phys. Chem. C 115 (2011) 5675–5682.
[79] S. Banerjee, J. Gopal, P. Muraleedharan, A.K. Tyagi, B. Raj, Curr. Sci. 90 (2006) 1378–1383.
[80] G.J. Snyder, E.S. Toberer, Nat. Mater. 7 (2008) 105–114.
[81] J.W. Tang, J.H. Ye, Chem. Phys. Lett. 410 (2005) 104–107.
[82] T.L. Bahers, M.R. rat, P. Sautet, J. Phys. Chem. C 118 (2014) 5997–6008.
[83] J. Sato, H. Kobayashi, Y. Inoue, J. Phys. Chem. B 107 (2003) 7970–7975.
[84] B. Xu, X. Li, G. Yu, J. Zhang, S. Ma, Y. Wang, L. Yi, J. Alloys Compd. 565 (2013) 22–28.
[85] T.J. Scheidemantel, C. Ambrosch-Draxl, T. Thonhauser, J.V. Badding, J.O. Sofo, Phys. Rev. B 2003, 68:125210(6).
[86] S. Sharma, S.K. Pandey, J. Phys. Condens. Matter. 26 (2014) 215501.
[87] A.H. Reshak, S. Azam, J. Magn. Magn. Mater. 342 (2013) 80–86.
[88] Chenming Calvin Hu, Modern Semiconductor Devices for Integrated Circuits, Part I: Electrons and holes in a semiconductor November 11, 2011.
[89] A.H. Reshak, S. Auluck, Computat Mater. Sci. 96 (2015) 90–95.
[90] A.H. Reshak, J. Phys. Chem. Solids 78 (2015) 46–52.
[91] A.H. Reshak, Renew. Energy 76 (2015) 36–44.
[92] A.H. Reshak, RSC Adv. 4 (2014) 63137;
A.H. Reshak, RSC Adv. 5 (2015) 47569.